nature physics

Article

https://doi.org/10.1038/s41567-023-01960-5

Quantum phase diagram of high-pressure hydrogen

Received: 4 May 2022

Accepted: 18 January 2023

Published online: 13 March 2023

Check for updates

Lorenzo Monacelli [1] ✉, Michele Casula [2] ✉, Kousuke Nakano[3,4], Sandro Sorella[4] & Francesco Mauri [1] ✉

Hydrogen is the most abundant element in the Universe. However, understanding the properties of dense hydrogen is still an open challenge because—under megabar pressures—the quantum nature of both electrons and protons emerges, producing deviations from the common behaviour of condensed-matter systems. Experiments are challenging and can access only limited observables, and the interplay between electron correlation and nuclear quantum motion makes standard simulations unreliable. Here we present the computed phase diagram of hydrogen and deuterium at low temperatures and high pressures using state-of-the-art methods to describe both many-body electronic correlation and quantum anharmonic motion of protons. Our results show that the long-sought atomic metallic hydrogen phase—predicted to host room-temperature superconductivity—forms at 577(4) GPa. The anharmonic vibrations of nuclei pushes the stability of this phase towards pressures much larger than previous estimates or attained experimental values. Before atomization, molecular hydrogen transforms from a metallic phase (phase III) to another metallic structure that is still molecular (phase VI) at 410(20) GPa. Isotope effects increase the pressures of both transitions by 63 and 32 GPa, respectively. We predict signatures in optical spectroscopy and d.c. conductivity that can be experimentally used to distinguish between the two structural transitions.

In 1968, Ashcroft predicted that atomic metallic hydrogen is a room-temperature superconductor[1]. During the last fifty years, a lot of effort was directed to synthesize atomic hydrogen in a laboratory under stable conditions. Nonetheless, the challenge proved more difficult than expected. Solid hydrogen at high pressures exhibits a very rich phase diagram with the presence of five different molecular phases, labelled from I to V (refs. [2–4]). Recently, a new phase transition has been observed above 420 GPa into a metallic state by infrared (IR) absorption measurements[5], namely, phase VI. An earlier work[6] measured the Raman spectra of hydrogen up to 480 GPa without incurring any evidence of a sudden change in the sample up to 450 GPa, where the Raman intensity drops. They also reported hydrogen to become metallic already in phase III at about 360 GPa. At even larger pressures, one work[7] claimed to have synthesized atomic metallic hydrogen on the basis of reflectivity measurements at 495 GPa, with the reflectivity data in good agreement with theoretical predictions[8], although the reliability of their observation has been questioned[9,10]. Further uncertainties come from technical difficulties in determining the pressure at these extreme conditions, which could lead to a mismatch of up to 80 GPa (ref. [11]), jeopardizing the possibility to reproduce results by independent studies.

The structural characterization of these phases is challenging since both neutron and X-ray diffraction experiments require sample sizes non-compatible with pressures larger than 250 GPa (ref. [12]) under hydrostatic conditions. Consequently, numerical ab initio simulations play a crucial role in understanding the phase diagram and can, in principle, address the following questions. Has atomic metallic hydrogen

[1]University of Rome, 'Sapienza', Dipartimento di Fisica, Rome, Italy. [2]Institut de Minéralogie, de Physique des Matériaux et de Cosmochimie, Sorbonne Université, Paris, France. [3]Japan Advanced Institute of Science and Technology (JAIST), Nomi, Japan. [4]International School for Advanced Studies (SISSA), Trieste, Italy. ✉e-mail: lorenzo92monacelli@gmail.com; michele.casula@impmc.upmc.fr; francesco.mauri@uniroma1.it

https://doi.org/10.1038/s41567-023-01960-5

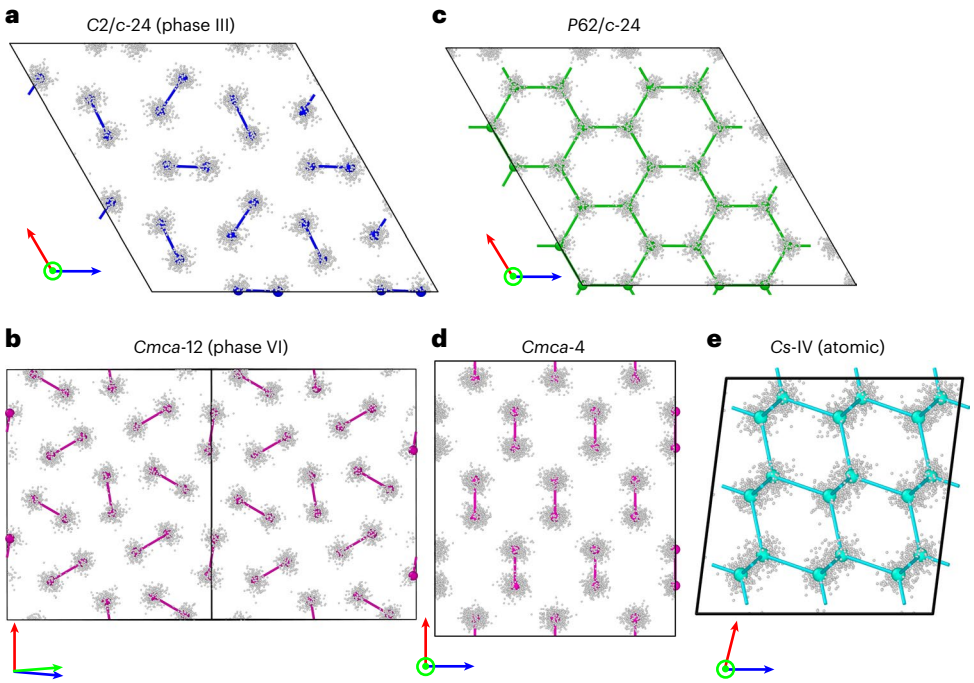

Fig. 1 | Structures considered for the low-temperature high-pressure phase diagram of hydrogen. a–**e**, Coloured balls are the average centroid positions, sticks represent the H_2 molecules and the cloud of smaller grey balls is a set of 250 configurations that sample the quantum probability distribution at 0 K. All the structures, apart from the atomic one, are made of layers, out of which we report only one. *P*62/*c*-24 is made of alternating layers, one with atoms arranged in a honeycomb lattice (**b**), and the other with molecular H_2 in a *C*2/*c*-24 arrangement (not reported here).

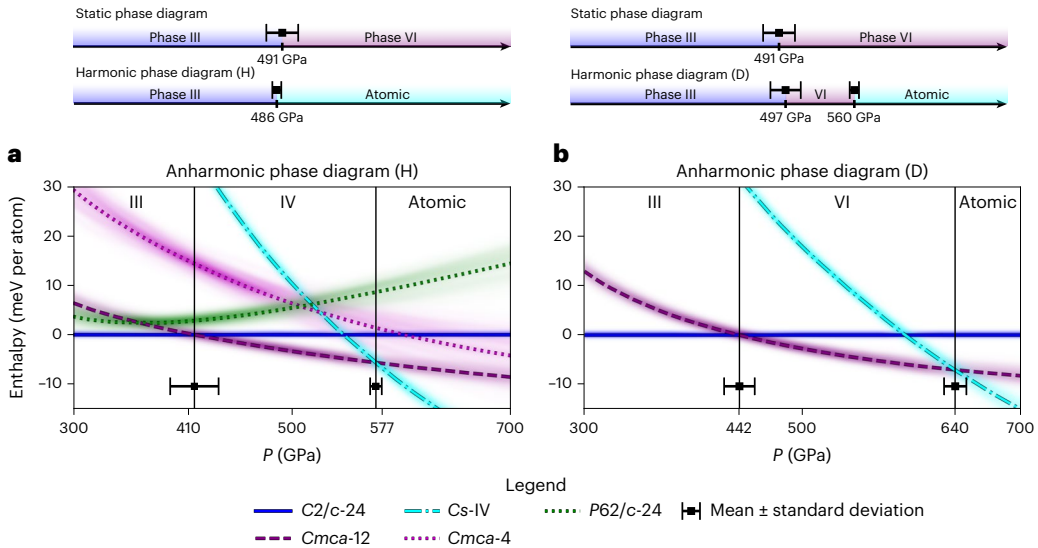

Fig. 2 | Phase diagram of hydrogen and deuterium. a,**b**, Phase diagram of hydrogen (H; **a**) and deuterium (D; **b**) at $T = 0$ K. Schematic of the phase diagram obtained by neglecting the nuclear zero-point energy (static lattice) and by employing the harmonic zero-point energy (top). For the final anharmonic phase diagram, we explicitly report the enthalpies of different phases with respect to phase III (*C*2/*c*-24). The most stable structure is the lowest in enthalpy at a given pressure. Enthalpies are evaluated at the DMC level. Hydrogen transforms from phase III (*C*2/*c*-24) to phase VI (*Cmca*-12) at 410 ± 20 GPa (442 ± 16 GPa for D), and then to the atomic superconductive phase (*Cs*-IV) at 577 ± 4 GPa (640 ± 9 GPa for D). Anharmonicity strongly affects the transition pressures and qualitatively affects the phase diagram of hydrogen. The transition pressures and their corresponding standard deviations are obtained using a bootstrap procedure. The raw data are randomized accounting for stochastic errors of SSCHA and DMC, and the phase diagram is recalculated for each set of randomized data. The shaded region around the mean enthalpy curves is plotted using this same procedure. More details on the precision and errors of the simulation are reported in Methods and Supplementary Information. Extended Data Figs. 1 and 2 illustrate how the enthalpies of the various phases evolve from the static to the quasi-harmonic approximation and finally to the full quantum SSCHA treatment at the DFT–BLYP and DMC levels, respectively.

been synthesized yet? At which pressure do we expect to stabilize it? What is the effect of isotope substitution?

Nevertheless, ab initio approaches have also been plagued so far by severe limitations. Indeed, as hydrogen is the lightest element, its nucleus is subject to huge quantum fluctuations that can largely affect its structural properties. Indeed, nuclear quantum effects have been shown to completely reshape the Born–Oppenheimer (BO) energy landscape in hydrogen-rich materials at high pressure[13–15],

https://doi.org/10.1038/s41567-023-01960-5

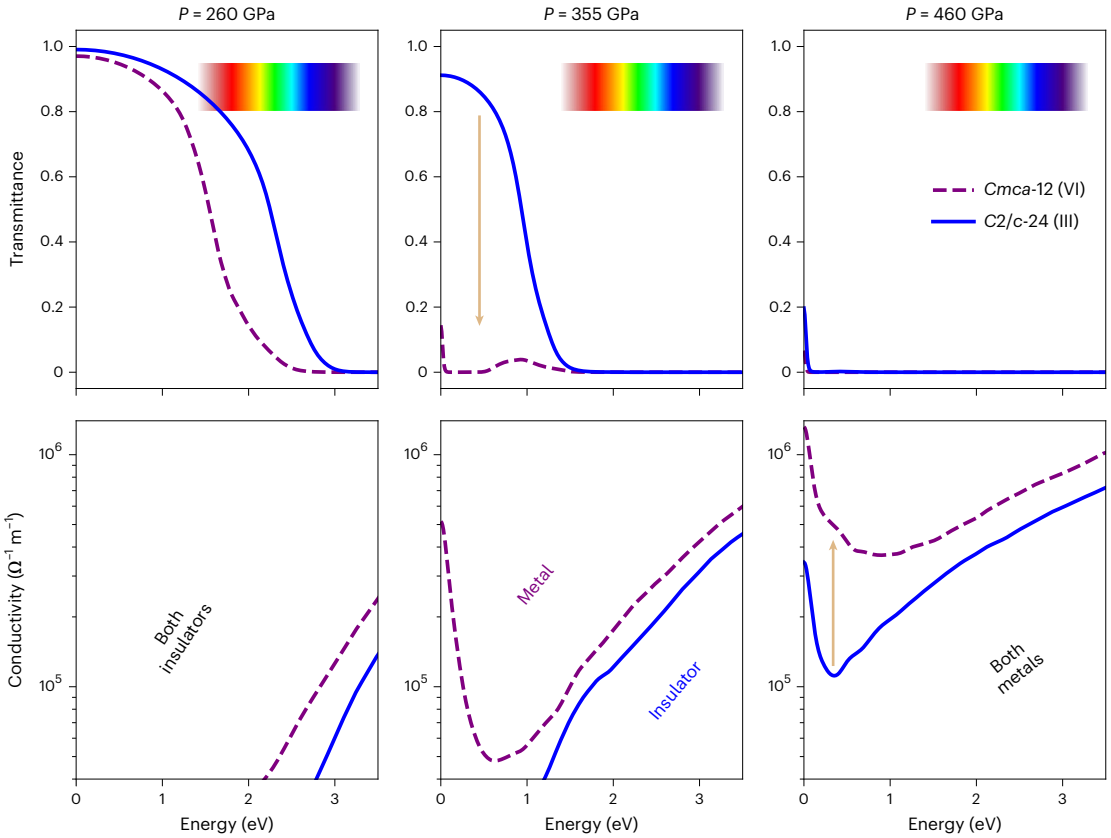

Fig. 3 | Simulation of transmittance and real part of optical conductivity at various pressures and comparing phase III (*C*2/*c*-24) with phase VI (*Cmca*-12). The rainbow colours match their respective energy in the visible spectrum. The arrows highlight differences in the optical properties between the two phases. We observe the transmittance of phase VI dropping down at lower energies than phase III. This phase is already completely opaque at 355 GPa. Also, the d.c. conductivity is higher in phase VI than phase III. The increase in conductivity around zero energy is the Drude peak and it is a signature of the indirect-bandgap closure (metallicity). The reported pressures correspond to volumes of 1.62, 1.42 and 1.25 Å^3 per H atom, and they are averaged over the two phases (the actual pressures differ at most by 5 GPa from the average). The reflectivity and electronic DOS in the same pressure range for these two phases are reported in Extended Data Fig. 3.

invalidating the phase diagram obtained with classical simulations. Furthermore, many competing structures differ in enthalpy by less than 1 meV per atom in a broad range of pressures[16]. This makes the identification of the ground state very sensitive to approximations, like the choice of the exchange–correlation functional in density functional theory (DFT) calculations. To overcome this issue, more sophisticated and accurate theories are required, such as the quantum Monte Carlo (QMC) methods[17]. For these reasons, the establishment of theoretical calculations fully accounting for both electron correlation energy and lattice anharmonicity at the same level of accuracy is fundamental to determine the hydrogen phase diagram at such high pressures.

To answer the aforementioned questions, we performed hydrogen phase diagram calculations at a methodological cutting edge, by combining the highly accurate description of electron correlation within diffusion quantum Monte Carlo (DMC) and the anharmonic lattice optimization accounting for nuclear quantum effects within the stochastic self-consistent harmonic approximation (SSCHA)[18–21]. DMC is a well-established framework that provides the most accurate internal energies of solid hydrogen[16,22–24]. Here it has been coupled to SSCHA in a seamless fashion with the aim of including both electronic and nuclear contributions in a non-perturbative way. The SSCHA algorithm has the advantage over other approximations[16,24,25] to be able to relax atomic positions, lattice vectors and phonon correlations, and its variational formulation ensures error compensation when comparing the free energy of different phases. The combination of these methods, coupled with a careful estimation of error bars, allows us to account for all the main ingredients needed to unveil the phase diagram of high-pressure hydrogen.

In our approach, SSCHA provides both vibrational energies and average nuclear positions (centroids), calculated from nuclear quantum fluctuations developed on top of a DFT Becke–Lee–Yang–Parr (BLYP)[26] energy landscape (Extended Data Figs. 1–8 and Supplementary Information provide more details about the precision of this DFT functional). The resulting crystal structure of the centroids is used to compute the DMC electronic internal energies, which are combined with the SSCHA zero-point energies of the anharmonic lattice.

We modelled phase III as the monoclinic *C*2/*c*-24 structure[27,28], which is the best representative of this phase (Fig. 1a). Other candidates that could represent phase III have been proposed over the years. However, *C*2/*c*-24 is the most stable in the high-pressure range we studied[29] and the one whose Raman, IR and optical signatures are in extremely good agreement with the experiments[30]. Hereafter, we will name crystal structures with their symmetry group followed by the number of atoms in the primitive cell, in line with previous literature.

Besides *C*2/*c*-24, we took into account the *Cmca*-12 crystalline symmetry (Fig. 1b), a new hexagonal structure with *P*62/*c*-24 symmetry (Fig. 1c) and the *Cmca*-4 structure (Fig. 1d) as the most promising molecular geometries for phase VI. *Cmca*-12 was first suggested as an alternative candidate for phase III (ref. [28]), and more recently proposed as phase VI (ref. [22]). *Cmca*-4 (ref. [28]) is the ground state in the harmonic DFT phase diagram with common functionals (Perdew–Burke–Ernzerhof and BLYP) over a large pressure range, but considerably disfavoured by

https://doi.org/10.1038/s41567-023-01960-5

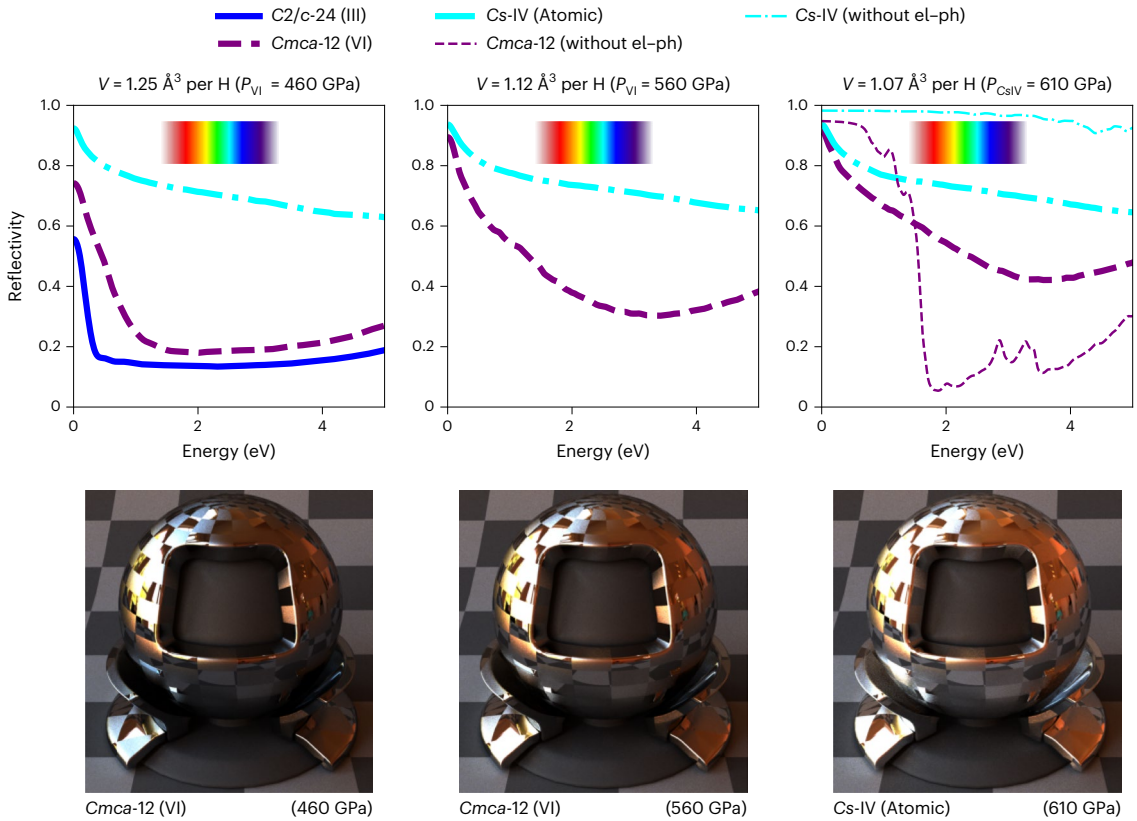

Fig. 4 | Reflectivity and photorealistic render of high-pressure metallic hydrogen. At the transition between phase III and phase VI, there is no visible jump in reflectivity under visible light, and the metal appears almost black (centre-bottom panel). As we increase the pressure, the reflectivity gradually increases until we reach the transition to the atomic phase, where we have a significant jump and the material appears shiny (bottom-right panel). In the top-right panel, we also report the reflectivity obtained without electron–phonon (el–ph) coupling (that is, a standard static calculation). Interestingly, in molecular phases, the electron–phonon coupling enhances the reflectivity by increasing the DOS at the Fermi level, whereas for atomic hydrogen, the electron–phonon interaction suppresses it. The data are calculated at the same volume for all the phases, and we show the pressure of the phase that is the ground state at that volume. The photorealistic render of the high-pressure hydrogen in vacuum is made by feeding the Mitsuba2 software[36] with the complex refractive index of hydrogen and introducing a texture to simulate both rough and smooth appearance, following the methodology discussed elsewhere[38]. The real and imaginary parts of conductivity for *Cmca*-12 (phase VI) and *Cs*-IV (atomic phase) in the same pressure range are reported in Extended Data Fig. 4.

the most accurate QMC internal energies[16,22]. We discovered the new *P*62/*c*-24 structure by relaxing the symmetry constraint on *C*2/*c*-24 with quantum anharmonic fluctuations above 320 GPa at the DFT–BLYP level of theory. It is made of graphene-like sheets alternating with molecular layers, conferring the phase with similar optical properties as graphite. It is a saddle point of the BO energy landscape, stabilized by quantum fluctuations (Supplementary Information). However, it turns out that this crystalline symmetry is also disfavoured by QMC energies.

Finally, we simulated the atomic phase *I*4/*amd*-2, also called *Cs*-IV (ref. [22]) (Fig. 1e). According to DFT, it is the most stable atomic symmetry beyond the molecular phases, and it is the one where room-temperature superconductivity has been predicted[31]. In Fig. 1, we report the centroid positions of these structures at 650 GPa with a visualization of the amplitude of quantum fluctuations. We neglected *mC*-24 (ref. [32]), stable between 450 and 600 GPa within the quasi-harmonic approximation and DFT–Perdew–Burke–Ernzerhof, because a preliminary study (Supplementary Information) unveils how DMC-corrected energies bring this phase to be significantly higher in energy than both *Cmca*-12 and *Cs*-IV.

We present the complete phase diagram for hydrogen (H) and deuterium (D) in Fig. 2a,b, respectively. Figure 2 (top) shows the schematic of the phase diagram computed by neglecting the nuclear zero-point motion (static lattice) and the one with harmonic zero-point energy.

Hydrogen transforms into an atomic metal at 577 ± 4 GPa, much above the pressure predicted neglecting anharmonicity. The isotope shift of this transition is one of the biggest ever reported, as deuterium transits into its atomic metallic state at 640 ± 9 GPa. Anharmonicity modifies the structure of all the molecular phases, stretching the molecular bonds and softening the H_2 molecular vibrations by about 1,000 cm^{-1} (ref. [30]). Thus, the relaxation of anharmonic energy strongly favours molecular phases, shifting the atomization pressure by more than 80 GPa compared with harmonic results. The phase boundaries identified here have a negligible dependence of temperature up to room temperature, where other phases—not considered here—may be favoured[16,24] from the entropy gain due to the thermal activation of H_2 rotations.

Even though the anharmonic contributions significantly impact the energy difference between molecular and atomic phases, the latter turns out not to be as harmonic as previously suggested[31]. Indeed, we found that *Cs*-IV exhibits prominent anharmonicity in the cell shape. The only free parameter of the *Cs*-IV structure is the *c*/*a* ratio of the tetragonal lattice. The anharmonicity increases the *c*/*a* ratio by about 0.12, independently of the pressure and level of electronic theory employed. A recent path integral molecular dynamics calculation also showed non-trivial anharmonicity in the *Cs*-IV phase[33] even at a fixed cell. The SSCHA is able to capture this anharmonicity, too, owing to recent advances in the technique[19]. The correct simulation of the *c*/*a* structural parameter has relevant consequences on the superconducting properties: by varying *c*/*a* at a fixed volume, *Cs*-IV undergoes a Lifshitz transition that enhances the density of states (DOS) at the

Fermi level. Quantum anharmonic fluctuations shift c/a away from the Lifshitz transition, preventing the enhancement in the superconducting critical temperature in the range of pressures where this phase is stable (Supplementary Information).

Before becoming an atomic metal, hydrogen undergoes another phase transition between two molecular phases (III→VI). This transition occurs at 410 ± 20 GPa for H (442 ± 16 GPa for D), in agreement with the experimental results discussed elsewhere[5]. The experimental marker of this phase transition is a sudden drop in transmittance in the near-IR region, ascribed to the closure of the direct bandgap in correspondence to a structural rearrangement. However, other experiments exploring the same pressure range observed the sample under visible light without spotting any trace of phase transition[6,10]. To investigate this situation, we computed the optical properties in the near-IR and visible range for phase III ($C2/c$-24) for the structure we predict to be stable above 422 GPa, namely, *Cmca*-12. Our calculations account for non-perturbative electron–phonon interactions. The electronic bands are computed within the modified Becke–Johnson meta-generalized gradient approximation[34], which shares a similar accuracy with hybrid functionals and self-consistent *GW* calculations, by following the same methodology discussed in another work[30]. We find that the *Cmca*-12 structure does not transmit light in the IR around the transition pressure, in contrast with phase III ($C2/c$-24) (Fig. 3). Our data explain the drop in IR transmittance observed in the experiment[5] and thus supports the assignment of phase VI to *Cmca*-12 symmetry. Moreover, phases III and VI display an almost identical low reflectivity in the visible window of 1.8–3.2 eV (Fig. 4); therefore, they are almost indistinguishable under visible light. This explains why experiments that explored the required pressure did not observe the phase transition[6,7]. We also predict a resistance drop at the phase transition, associated with an increase in the electronic DOS at the Fermi level. Conductivity measurements on hydrogen[6] stop just before the transition pressure. The sudden rise in conductivity is an independent feature that can unambiguously prove the transition to phase VI. Our results differ from a previous theoretical work[35], which adopted a simulation cell of 96 atoms, a different exchange–correlation potential (HSE06) and sampled only electron–hole excitations where interactions with phonons outside the centre of the Brillouin zone are not accounted for (Supplementary Information).

In Fig. 4, we report the reflectivity data for phases III, VI and atomic one as the pressure increases. At each pressure, we show a photorealistic render of a high-pressure solid hydrogen sample in vacuum, simulated by solving the Fresnel equation as implemented in the Mitsuba2 software[36]. Phase VI becomes gradually more reflective on increasing the pressure, until it transforms into atomic *Cs*-IV at about 577 GPa, where it becomes shiny, reflecting almost 80% of visible light. Despite being significantly attenuated by vibrational disorder, the sudden rise in reflectivity in visible light is a key signature of the molecular-to-atomic transition. Together with reflectivity, the static conductivity also gradually increases on loading pressure and jumps to a higher value at the transition to the atomic *Cs*-IV phase (Supplementary Information). In contrast to phase VI, the atomic phase shows no significant variation in reflectivity and conductivity with pressure. Interestingly, the quantum nuclear fluctuations have an opposite effect on molecular phases, where they enhance reflectivity, compared with the atomic phase in which reflectivity is strongly suppressed. The suppression of reflectivity in the atomic phase was already found in other works[8,37].

In conclusion, the hydrogen phase diagram based on both highly accurate electronic internal energies computed by QMC and anharmonic nuclear quantum fluctuations provided by SSCHA confirms that hydrogen undergoes a first-order phase transition from conductive phase III (molecular $C2/c$-24) to metallic phase VI (molecular *Cmca*-12) at 410 ± 20 GPa, in accordance with experiments[5], with an isotope shift of 32 GPa towards higher pressure. We predict the transition towards atomic metallic hydrogen to occur at 577 GPa, with an isotope shift of 63 GPa to even higher pressures. Even if we cannot exclude the existence of new stable phases yet to be discovered, our predicted hydrogen *Cs*-IV atomization pressure is a robust lower bound that poses a great experimental challenge for its synthesis and calibration.

Online content

Any methods, additional references, Nature Portfolio reporting summaries, source data, extended data, supplementary information, acknowledgements, peer review information; details of author contributions and competing interests; and statements of data and code availability are available at https://doi.org/10.1038/s41567-023-01960-5.

References

1. Ashcroft, N. W. Metallic hydrogen: a high-temperature superconductor? *Phys. Rev. Lett.* **21**, 1748–1749 (1968).
2. Mao, H.-k & Hemley, R. J. Ultrahigh-pressure transitions in solid hydrogen. *Rev. Mod. Phys.* **66**, 671 (1994).
3. Howie, R. T., Guillaume, C. L., Scheler, T., Goncharov, A. F. & Gregoryanz, E. Mixed molecular and atomic phase of dense hydrogen. *Phys. Rev. Lett.* **108**, 125501 (2012).
4. Dalladay-Simpson, P., Howie, R. T. & Gregoryanz, E. Evidence for a new phase of dense hydrogen above 325 gigapascals. *Nature* **529**, 63–67 (2016).
5. Loubeyre, P., Occelli, F. & Dumas, P. Synchrotron infrared spectroscopic evidence of the probable transition to metal hydrogen. *Nature* **577**, 631–635 (2020).
6. Eremets, M. I., Drozdov, A. P., Kong, P. P. & Wang, H. Semimetallic molecular hydrogen at pressure above 350 GPa. *Nat. Phys.* **15**, 1246–1249 (2019).
7. Dias, R. P. & Silvera, I. F. Observation of the Wigner-Huntington transition to metallic hydrogen. *Science* **355**, 715–718 (2017).
8. Borinaga, M., Ibañez-Azpiroz, J., Bergara, A. & Errea, I. Strong electron-phonon and band structure effects in the optical properties of high pressure metallic hydrogen. *Phys. Rev. Lett.* **120**, 057402 (2018).
9. Goncharov, A. F. & Struzhkin, V. V. Comment on 'observation of the Wigner-Huntington transition to metallic hydrogen'. *Science* **357**, eaam9736 (2017).
10. Silvera, I. F. & Dias, R. Response to comment on 'observation of the Wigner-Huntington transition to metallic hydrogen'. *Science* **357**, eaan2671 (2017).
11. Loubeyre, P., Occelli, F. & Dumas, P. Comment on: observation of the Wigner-Huntington transition to metallic hydrogen. Preprint at https://arxiv.org/abs/1702.07192 (2017).
12. Ji, C. et al. Ultrahigh-pressure isostructural electronic transitions in hydrogen. *Nature* **573**, 558–562 (2019).
13. Straus, D. M. & Ashcroft, N. W. Self-consistent structure of metallic hydrogen. *Phys. Rev. Lett.* **38**, 415–418 (1977).
14. Errea, I. et al. High-pressure hydrogen sulfide from first principles: a strongly anharmonic phonon-mediated superconductor. *Phys. Rev. Lett.* **114**, 157004 (2015).
15. Errea, I. et al. Quantum crystal structure in the 250-kelvin superconducting lanthanum hydride. *Nature* **578**, 66–69 (2020).
16. Drummond, N. D. et al. Quantum Monte Carlo study of the phase diagram of solid molecular hydrogen at extreme pressures. *Nat. Commun.* **6**, 7794 (2015).
17. Foulkes, W. M. C., Mitas, L., Needs, R. J. & Rajagopal, G. Quantum Monte Carlo simulations of solids. *Rev. Mod. Phys.* **73**, 33–83 (2001).
18. Errea, I., Calandra, M. & Mauri, F. Anharmonic free energies and phonon dispersions from the stochastic self-consistent harmonic approximation: application to platinum and palladium hydrides. *Phys. Rev. B* **89**, 064302 (2014).

19. Bianco, R., Errea, I., Paulatto, L., Calandra, M. & Mauri, F. Second-order structural phase transitions, free energy curvature, and temperature-dependent anharmonic phonons in the self-consistent harmonic approximation: theory and stochastic implementation. *Phys. Rev. B* **96**, 014111 (2017).
20. Monacelli, L., Errea, I., Calandra, M. & Mauri, F. Pressure and stress tensor of complex anharmonic crystals within the stochastic self-consistent harmonic approximation. *Phys. Rev. B* **98**, 024106 (2018).
21. Monacelli, L. et al. The stochastic self-consistent harmonic approximation: calculating vibrational properties of materials with full quantum and anharmonic effects. *J. Phys.: Condens. Matter* **33**, 363001 (2021).
22. McMinis, J., Clay, R. C., Lee, D. & Morales, M. A. Molecular to atomic phase transition in hydrogen under high pressure. *Phys. Rev. Lett.* **114**, 105305 (2015).
23. Azadi, S., Drummond, N. D. & Foulkes, W. M. C. Nature of the metallization transition in solid hydrogen. *Phys. Rev. B* **95**, 035142 (2017).
24. Monserrat, B. et al. Structure and metallicity of phase V of hydrogen. *Phys. Rev. Lett.* **120**, 255701 (2018).
25. Azadi, S., Monserrat, B., Foulkes, W. M. C. & Needs, R. J. Dissociation of high-pressure solid molecular hydrogen: a quantum Monte Carlo and anharmonic vibrational study. *Phys. Rev. Lett.* **112**, 165501 (2014).
26. Miehlich, B., Savin, A., Stoll, H. & Preuss, H. Results obtained with the correlation energy density functionals of Becke and Lee, Yang and Parr. *Chem. Phys. Lett.* **157**, 200–206 (1989).
27. Kohanoff, J., Scandolo, S., de Gironcoli, S. & Tosatti, E. Dipole-quadrupole interactions and the nature of phase III of compressed hydrogen. *Phys. Rev. Lett.* **83**, 4097–4100 (1999).
28. Pickard, C. J. & Needs, R. J. Structure of phase III of solid hydrogen. *Nat. Phys.* **3**, 473–476 (2007).
29. Azadi, S. & Kühne, T. D. Unconventional phase III of high-pressure solid hydrogen. *Phys. Rev. B* **100**, 155103 (2019).
30. Monacelli, L., Errea, I., Calandra, M. & Mauri, F. Black metal hydrogen above 360 GPa driven by proton quantum fluctuations. *Nat. Phys.* **17**, 63–67 (2020).
31. Borinaga, M., Errea, I., Calandra, M., Mauri, F. & Bergara, A. Anharmonic effects in atomic hydrogen: superconductivity and lattice dynamical stability. *Phys. Rev. B* **93**, 174308 (2016).
32. Liu, H., Wang, H. & Ma, Y. Quasi-molecular and atomic phases of dense solid hydrogen. *J. Phys. Chem. C* **116**, 9221–9226 (2012).
33. Morresi, T., Paulatto, L., Vuilleumier, R. & Casula, M. Probing anharmonic phonons by quantum correlators: a path integral approach. *J. Chem. Phys.* **154**, 224108 (2021).
34. Tran, F. & Blaha, P. Accurate band gaps of semiconductors and insulators with a semilocal exchange-correlation potential. *Phys. Rev. Lett.* **102**, 226401 (2009).
35. Gorelov, V., Holzmann, M., Ceperley, D. M. & Pierleoni, C. Energy gap closure of crystalline molecular hydrogen with pressure. *Phys. Rev. Lett.* **124**, 116401 (2020).
36. Nimier-David, M., Vicini, D., Zeltner, T. & Jakob, W. Mitsuba 2: a retargetable forward and inverse renderer. *ACM Trans. Graph.* **38**, 203 (2019).
37. Zhang, C. et al. Finite-temperature infrared and Raman spectra of high-pressure hydrogen from first-principles molecular dynamics. *Phys. Rev. B* **98**, 144301 (2018).
38. Prandini, G., Rignanese, G.-M. & Marzari, N. Photorealistic modelling of metals from first principles. *Mater.* **5**, 129 (2019).

Methods

We first describe how the phase diagram is computed when we adopt a different electronic theory—DFT versus DMC—with and without quantum anharmonicity.

We relaxed each structure by including quantum fluctuations and anharmonicity through SSCHA, optimizing the auxiliary force constants, centroid positions and lattice vectors within the constraints of the symmetry group, roughly at every 100 GPa (from 250 to 650 GPa). The SSCHA framework accounts for nuclear quantum fluctuations neglecting exchange effects, which we expect to be negligible in the range of pressures analysed here.

The SSCHA optimizes a Gaussian ansatz for the nuclear density matrix, which represents the quantum anharmonic equilibrium distribution of ions, to minimize the free energy. Within this framework, one can relax the lattice vectors, average atomic positions and correlated nuclear fluctuations. More details are provided elsewhere[21].

In the SSCHA calculations, we employed the DFT framework with the BLYP exchange–correlation functional[26] to account for electronic energy and determine the surface of the BO potential energy. BLYP is one of the most accurate DFT functionals for phase diagram calculations of high-pressure hydrogen, outperforming more refined techniques such as hybrid DFT[16,39], and very similar to the van der Waals-based VDW-DF functional. The total anharmonic energy is obtained within DFT by fitting the difference between BO energy and SSCHA total energy at fixed volumes for each phase with a parabola. Also, the anharmonic stress tensor is included in the fit to increase the accuracy. We then add to the static BO-energy-versus-volume curves, roughly computed in DFT at every 5 GPa, the quantum anharmonic lattice vibrational contribution at the corresponding volume calculated from the fit. We finally perform the Legendre transform to get the enthalpy-versus-pressure curves and the resulting phase diagram.

The static phase diagram simulated within DFT–BLYP is reported in Extended Data Fig. 1a, whereas Extended Data Fig. 1b,c shows the DFT–BLYP phase diagram with harmonic zero-point energy. We included the harmonic contributions only for the most relevant phases: *C*2/*c*-24, *Cmca*-12 and *Cs*-IV. The harmonic zero-point energy leaves the pressure of *C*2/*c*-24-to-*Cmca*-12 transition (III-to-VI phase transition) almost unchanged, whereas it substantially shifts the atomic transition down to pressures even lower than the transition to the *Cmca*-12 structure. The results of the anharmonic phase diagram of both hydrogen (protium (^{1}H) or H) and deuterium (^{2}H or D) computed by DFT–BLYP and SSCHA are reported in Extended Data Fig. 1d,e. They show that anharmonicity strongly favours the molecular phases over the atomic one, shifting back the atomic transition to higher pressures. Between *Cmca*-12 and *C*2/*c*-24, anharmonicity favours the *Cmca*-12 crystal symmetry, moving the III-to-VI phase transition down by about 150 GPa. In this case, phase VI candidates, namely, *P*62/*c*-24, *Cmca*-12 and *Cmca*-4, are almost degenerate up to 400 GPa, where *Cmca*-4 starts dominating over the other molecular phases. Apart from *Cmca*-4, the DFT–BLYP phase diagram is in qualitative agreement with the electron correlation treated at the QMC level, and it shows a phonon spectrum almost completely coincident with the DFT–VDW-DF functional, with a difference in zero-point energy of about 0.3 meV H^{-1} (Extended Data Fig. 5). This justifies the choice of BLYP to compute the anharmonic and zero-point energy contributions to the total enthalpies.

Owing to the extensive DMC calculations performed at fixed structures for several phases and volumes, we have been able to correct the DFT–BLYP internal energies and add the contribution coming from a nearly exact treatment of electron correlation on top of static, harmonic and quantum anharmonic phase diagrams previously computed at the DFT–BLYP level. DMC corrections are evaluated as the difference between DFT–BLYP and DMC energies for each simulated volume and phase on the average position of centroids relaxed within SSCHA and with hydrogen mass. These corrections are added to the total-energy-versus-volume curves of the corresponding DFT (and DFT–SSCHA) calculations. As in the DFT case, the enthalpy-versus-pressure curves are obtained by the Legendre transform. The possible sources of error in our approach are the use of a constant correction between DMC and DFT depending only on phase and thermodynamic conditions, the choice of DFT functional for the SSCHA calculation, the failure of SSCHA in describing H_2 free rotations and the finite-size dependence of SSCHA results. We checked how each one of these approximations could individually affect the predicted phase diagram. The constant energy shift between DFT and DMC introduces the dominant error, which we tested by replacing the geometry of H centroids with those of D (Supplementary Tables 4 and 5 and Supplementary Fig. 17). Here we estimate an error of 20 GPa for the molecular phase transition (similar to stochastic error) and an error of 40 GPa towards higher pressures for the atomic phase. All the other sources of error are negligible or comparable to the stochastic error reported in Fig. 2; their analysis is shown in Extended Data Figs. 5 and 6 and Supplementary Fig. 15.

We report the static DMC-corrected phase diagram (Extended Data Fig. 2a) and the DMC-corrected enthalpies accounting for the nuclear zero-point energy within the harmonic approximation (Extended Data Fig. 2b,c). The final data that also include the anharmonic correction are shown in Fig. 2 and Extended Data Fig. 2d,e.

In Supplementary Information, we report further details on how the *P*62/*c*-24 structure has been discovered. This arises from an instability of the *C*2/*c*-24 phase when quantum anharmonic effects are included in the calculation (Supplementary Fig. 1). We have also studied the atomic *Cs*-IV phase stability as a function of cell shape (Supplementary Figs. 2 and 8) and the appearance of a Lifshitz transition in the *Cs*-IV phase (Supplementary Figs. 3–7). The sensitiveness of the Lifshitz transition determination with respect to the smearing scheme is studied in Supplementary Table 1. In Supplementary Fig. 3, we show the change in Fermi surface topology as *c*/*a* moves, which opens new pockets at the edges of the Fermi surface. We then show how the *mC*-24 structure, another semi-molecular crystal that has been predicted to be competitive above 450 GPa (ref. [32]), can be disregarded after BLYP–DMC calculations (Supplementary Fig. 9).

In addition, we provide the real and imaginary parts of optical conductivity for *Cmca*-12 and *Cs*-IV at higher pressures (Extended Data Fig. 4), as well as a convergence study of the simulated optical properties with respect to *k*-mesh sampling, electronic temperature and smearing (Supplementary Figs. 10–12).

DFT technical specifications are provided in Supplementary Information. The QUANTUM ESPRESSO software[40,41] has been used for our DFT calculations. In particular, we studied the DFT–BLYP total energy convergence with respect to *k*-mesh sampling and smearing for those phases having the largest DOS at the Fermi surface, namely, *Cmca*-4 and *Cs*-IV; this convergence study is reported in Supplementary Figs. 13 and 14, respectively. The converged *k*-mesh finally used in our self-consistent DFT and SSCHA calculations is specified in Supplementary Table 2 for each phase considered in the present work.

Finally, precise details on the DMC calculations are reported in Extended Data Figs. 1–8 and Supplementary Information. The QMC TurboRVB software[42] has been used for these calculations. Extended Data Fig. 7 shows the finite-size scaling of the DMC total energies, for each phase and volume. The stochastic DMC error bars comprise the uncertainty coming from extrapolation to the thermodynamic limit. The fixed-node gain coming from the QMC wave-function optimization can be found in Supplementary Table 3, and it has been included in the final DMC-corrected energies. We then report the volume/phase dependence of DFT–BLYP correction provided by our DMC calculations in Extended Data Fig. 8 and Supplementary Fig. 16, for both H and D geometries. As mentioned before, an estimate of the geometry dependence of DMC-based corrections is shown in Supplementary Fig. 17, where the DFT–BLYP energies have been corrected with D

structures taken as reference, instead of H. The corresponding transition pressures are reported in Supplementary Tables 4 and 5.

Data availability

The structures employed in the calculation, including the new $P62/c$-24 crystalline symmetry obtained after structural relaxation with quantum anharmonicity, are freely available via Materials Cloud[43]. All other data are available from the corresponding authors upon reasonable request from L.M. and M.C.

Code availability

The SSCHA and QUANTUM ESPRESSO codes used in this research are open source: the SSCHA suite can be downloaded from www.sscha.eu and the QMC TurboRVB package is available upon request from M.C. (michele.casula@upmc.fr) or K.N. (kousuke_1123@icloud.com).

References

39. Clay, R. C. et al. Benchmarking exchange-correlation functionals for hydrogen at high pressures using quantum Monte Carlo. *Phys. Rev. B* **89**, 184106 (2014).
40. Giannozzi, P. et al. QUANTUM ESPRESSO: a modular and open-source software project for quantum simulations of materials. *J. Phys.: Condens. Matter* **21**, 395502 (2009).
41. Giannozzi, P. et al. Advanced capabilities for materials modelling with quantum ESPRESSO. *J. Phys.: Condens. Matter* **29**, 465901 (2017).
42. Nakano, K. et al. TurboRVB: a many-body toolkit for ab initio electronic simulations by quantum Monte Carlo. *J. Chem. Phys.* **152**, 204121 (2020).
43. Monacelli, L., Casula, M., Nakano, K., Sorella, S. & Mauri, F. Quantum phase diagram of high-pressure hydrogen. *Materials Cloud* https://doi.org/10.24435/MATERIALSCLOUD:R1-WK (2022).

Acknowledgements

L.M. acknowledges CINECA under the ISCRA initiative for providing high-performance computational (HPC) resources employed in this work, and PRACE for providing computational resources under project no. ra0020 on Joliot-Curie Rome at TGCC, France. M.C. thanks GENCI for providing computational resources under grant no. 0906493, the Grands Challenge DARI for allowing calculations on the Joliot-Curie Rome HPC cluster under project no. gch0420. M.C., K.N. and S.S. thank RIKEN for providing computational resources of the supercomputer Fugaku through the HPCI System Research Projects (project IDs, hp210038 and hp220060). K.N. acknowledges support from the JSPS Overseas Research Fellowships, Grant-in-Aid for Early Career Scientists (grant no. JP21K17752) and Grant-in-Aid for Scientific Research (grant no. JP21K03400). S.S. acknowledges support from MIUR, PRIN-2017BZPKSZ. This work was supported by the European Centre of Excellence in Exascale Computing TREX: Targeting Real Chemical Accuracy at the Exascale. This project has received funding from the European Union's Horizon 2020 research and innovation programme under grant agreement no. 952165.

Author contributions

L.M., M.C. and F.M. conceived the work, and L.M. conducted all the DFT and SSCHA simulations, including those for the optical properties. M.C. and S.S. performed the QMC calculations, and M.C. and L.M. collaborated on analysing the results to derive the final phase diagram for hydrogen. Additionally, K.N. and S.S. contributed to develop the QMC TurboRVB software that enabled the large-scale calculations performed in this work. All the authors participated in writing the paper.

Competing interests

The authors declare no competing interests.

Additional information

Extended data is available for this paper at https://doi.org/10.1038/s41567-023-01960-5.

Supplementary information The online version contains supplementary material available at https://doi.org/10.1038/s41567-023-01960-5.

Correspondence and requests for materials should be addressed to Lorenzo Monacelli, Michele Casula or Francesco Mauri.

Peer review information *Nature Physics* thanks Xin-Zheng Li and the other, anonymous, reviewer(s) for their contribution to the peer review of this work.

https://doi.org/10.1038/s41567-023-01960-5

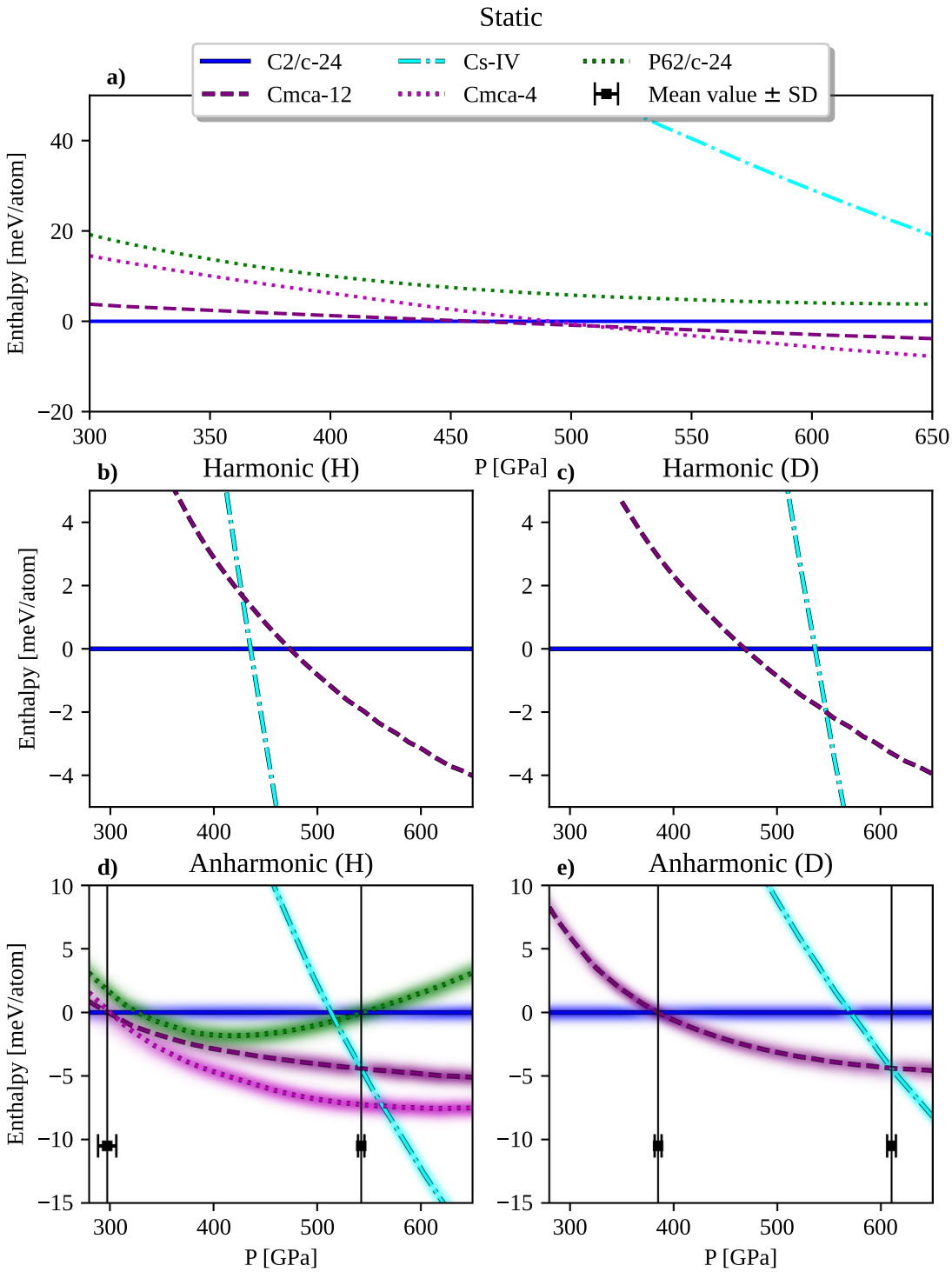

Extended Data Fig. 1 | DFT-BLYP phase diagram of high-pressure hydrogen. The static lattice enthalpies are in panel (**a**). We report the quasi-harmonic phase-diagram of hydrogen (panel **b**) and deuterium (panel **c**). The main structures (Cmca-12, C2/c-24 and Cs-IV) are reported in all panels. In panel **d**, we show the anharmonic (SSCHA) entalpies of hydrogen. Shaded area represent the bootstrap procedure: raw data from simulations are randomized with a normal distribution to represent the stochastic error of the SSCHA free energy and pressure. Each randomized data is displayed as a shaded line. Errors on the transition pressures are the standard deviation over the randomized data. Panel **e** reports the anharmonic enthalpy of deuterium.

https://doi.org/10.1038/s41567-023-01960-5

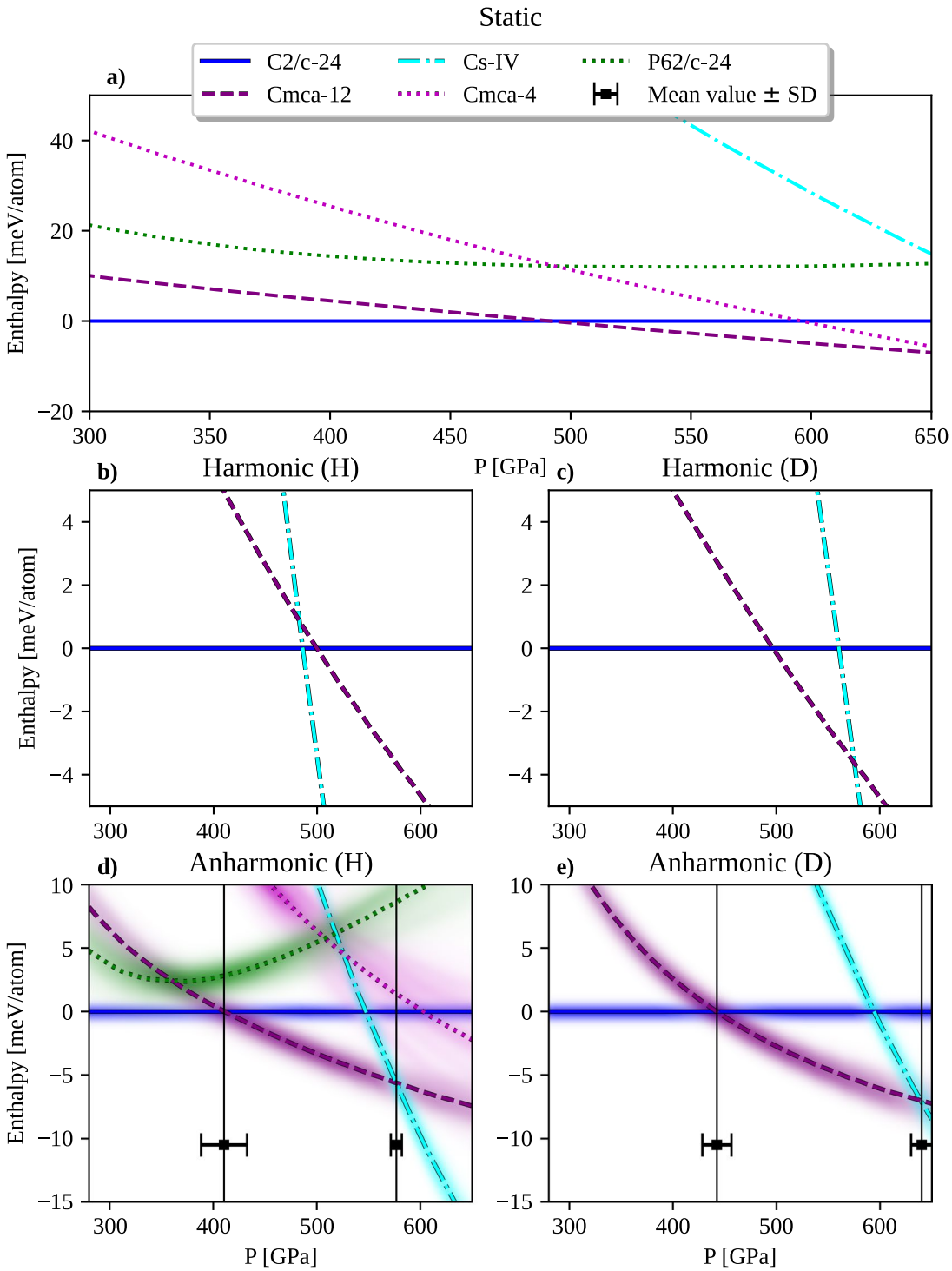

Extended Data Fig. 2 | DMC phase diagram of high-pressure hydrogen. This is an extended version of Fig. 2, where we report the enthalpies also for the static and harmonic phase-diagrams. The static lattice enthalpy is in panel **a**. Quasi-harmonic phase-diagram of hydrogen is reported in panel **b** (in panel **c** for deuterium). The main structures (Cmca-12, C2/c-24 and Cs-IV) are shown in all panels. In panel **c**, we report the quasi-harmonic phase diagram of deuterium. In panel **d**, we show the anharmonic (SSCHA) entalpies of hydrogen. This is the same as Fig. 2a. Anharmonic entalpies of deuterium are plotted in panel **e**, the same as Fig. 2b.

https://doi.org/10.1038/s41567-023-01960-5

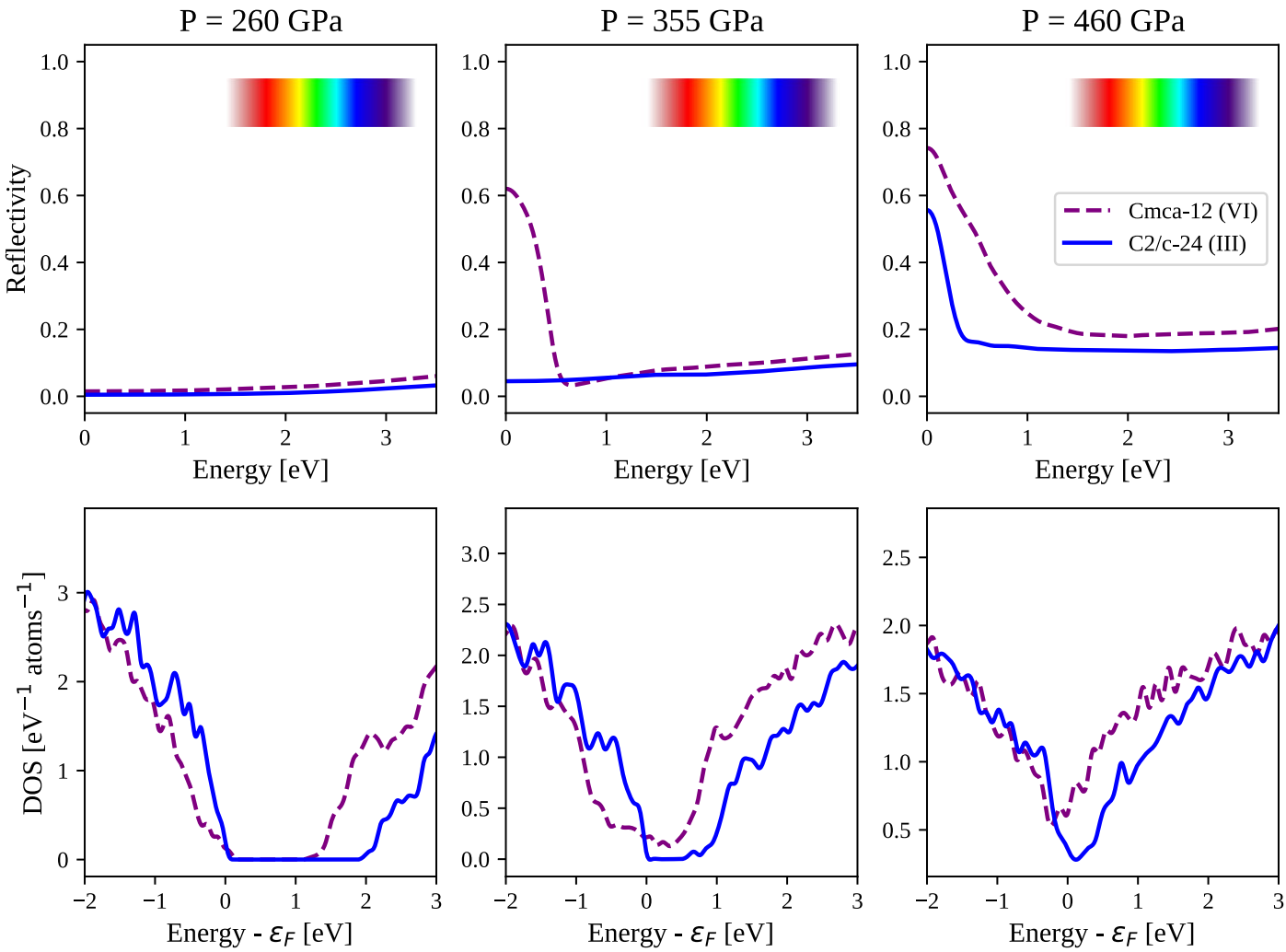

Extended Data Fig. 3 | Reflectivity (upper row) and DOS (lower row) of phase III (C2/c-24) and phase VI (Cmca-12) at different pressures. The pressures reported correspond to volumes of 1.62 Å^3,1.42 Å^3 and 1.25 Å^3 per H atom, and they are averaged over the two phases (the actual pressures differ at most by 5 GPa from the average).

https://doi.org/10.1038/s41567-023-01960-5

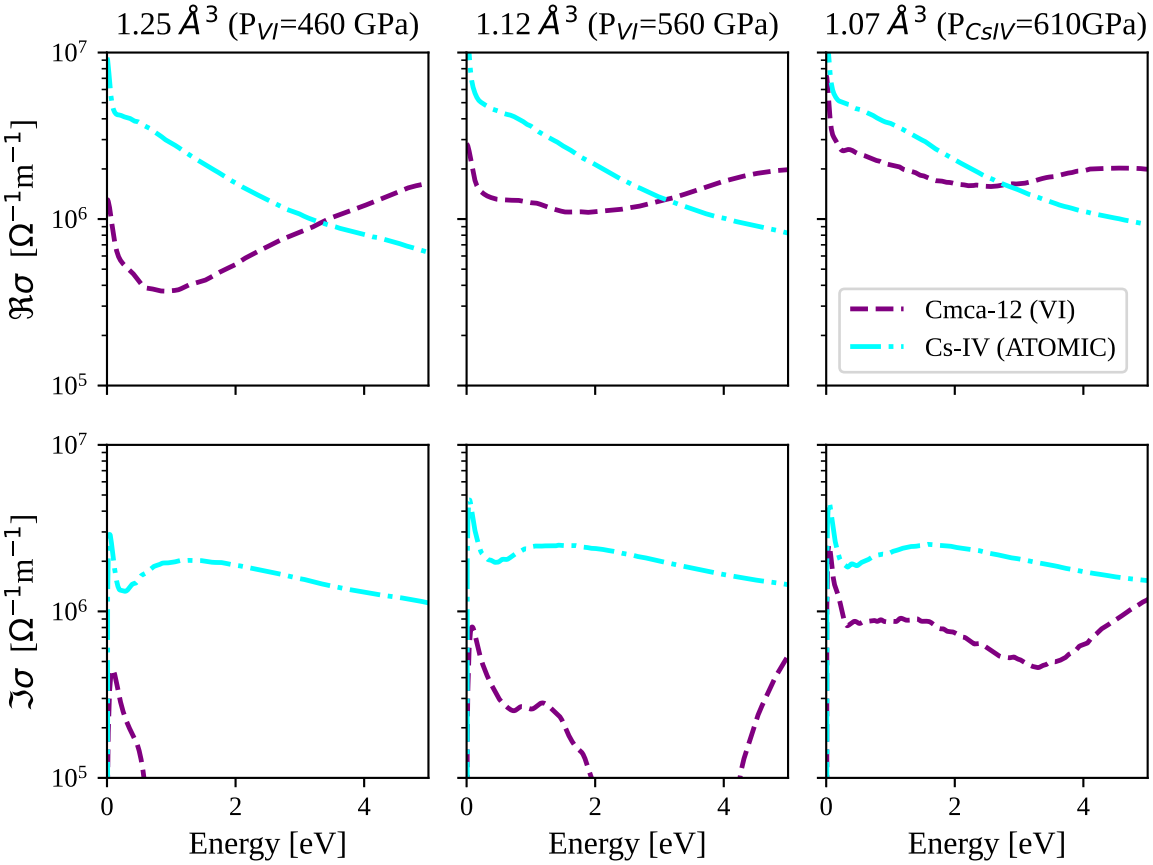

Extended Data Fig. 4 | Real (upper panels) and imaginary (lower panels) part of the conductivity of Cmca-12 and Cs-IV phases. The simulations are performed at constant volumes of 1.25 Å^3, 1.12 Å^3, 1.06 Å^3 per H atom, as those in Fig. 3, and the corresponding pressure reported refers to the value for the most stable structure at that volume.

https://doi.org/10.1038/s41567-023-01960-5

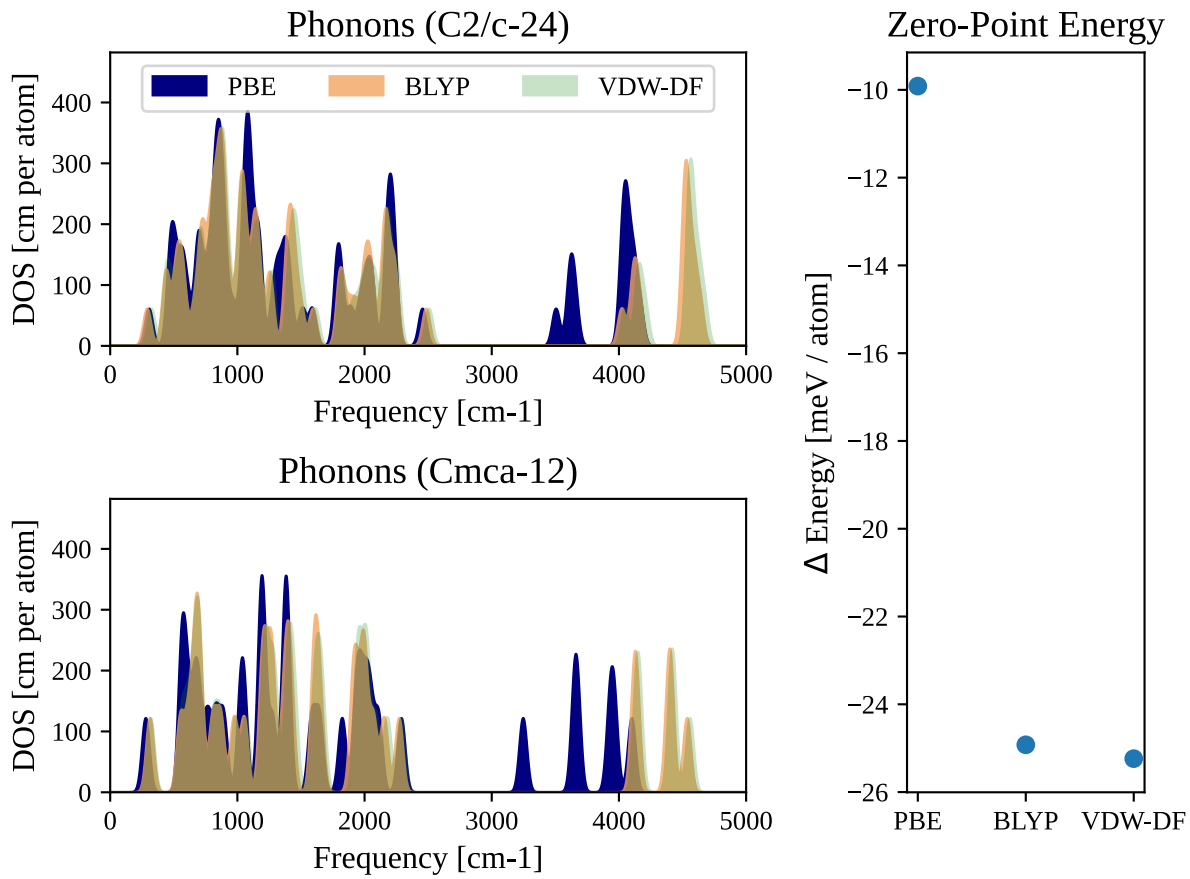

Extended Data Fig. 5 | Comparison of zero-point energy with different DFT functionals. Phonon DOS of C2/c-24 and Cmca-12 crystalline symmetries, and zero-point energy (ZPE) difference between the two, computed with PBE, BLYP and VDW-DF functionals. Both DOS and ZPE are evaluated only at Γ. While PBE strongly underestimates the vibron frequencies and the absolute value of the ZPE difference, BLYP and VDW-DF yield almost identical results.

https://doi.org/10.1038/s41567-023-01960-5

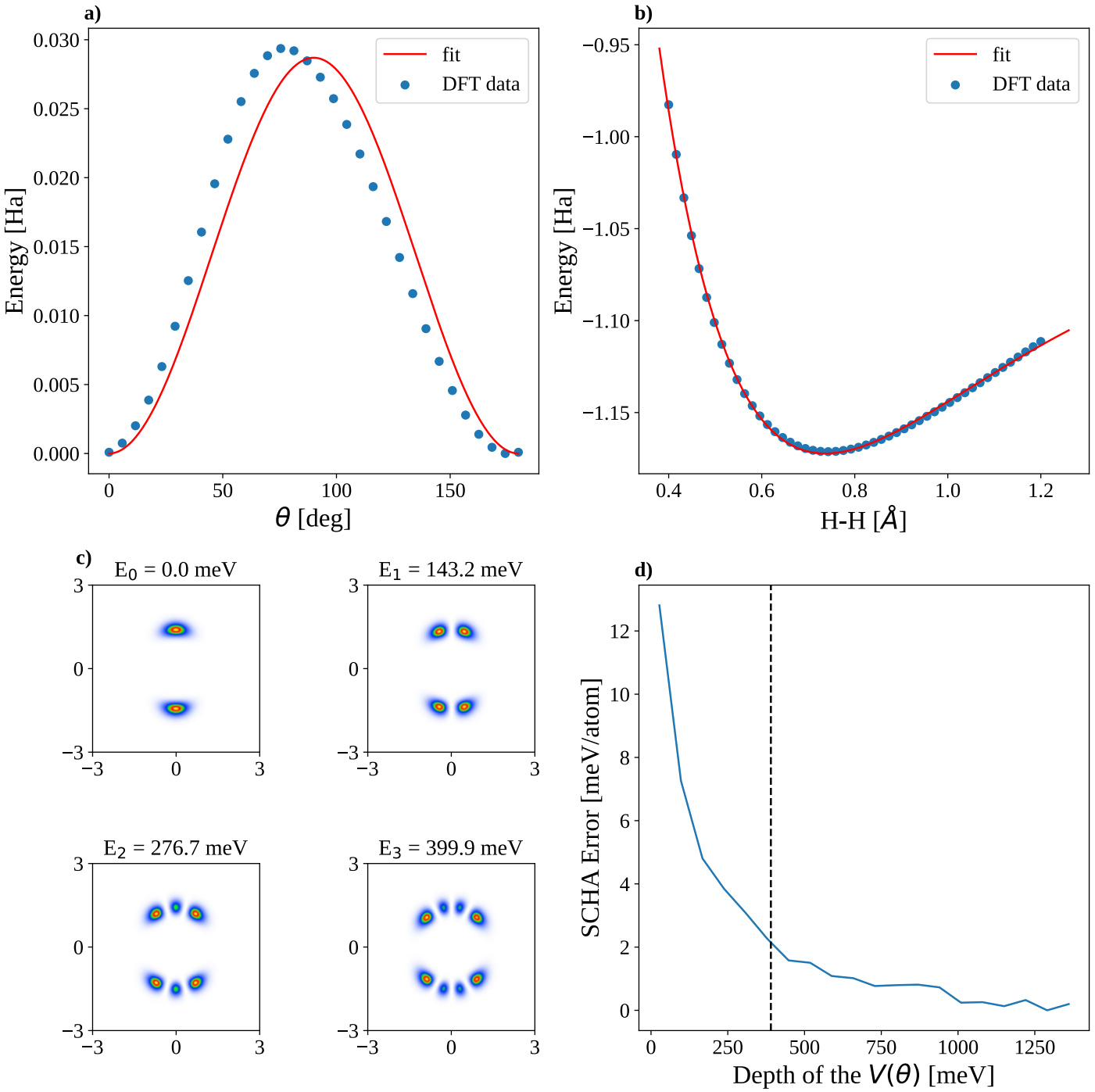

Extended Data Fig. 6 | Rotational degrees of freedom in Cmca-12. In panel **a**, we report the fit of the DFT-BLYP energy landscape for the rotation of one H_2 molecule inside the Cmca-12 structure at 350 GPa. The intramolecular H_2 potential is fitted with a Morse function in panel **b**. In panel **c**, we report the probability distribution of the reduced coordinate in the center-of-mass frame solved with the implicitly-restarted Lanczos algorithm (ground state and first excited states). Axes are in Bohr. The difference between the SSCHA ZPE and the exact ground-state as a function of the amplitude of the angular potential modulation is reported in panel **d**. The dashed line represent the value of the fit in panel **a**.

https://doi.org/10.1038/s41567-023-01960-5

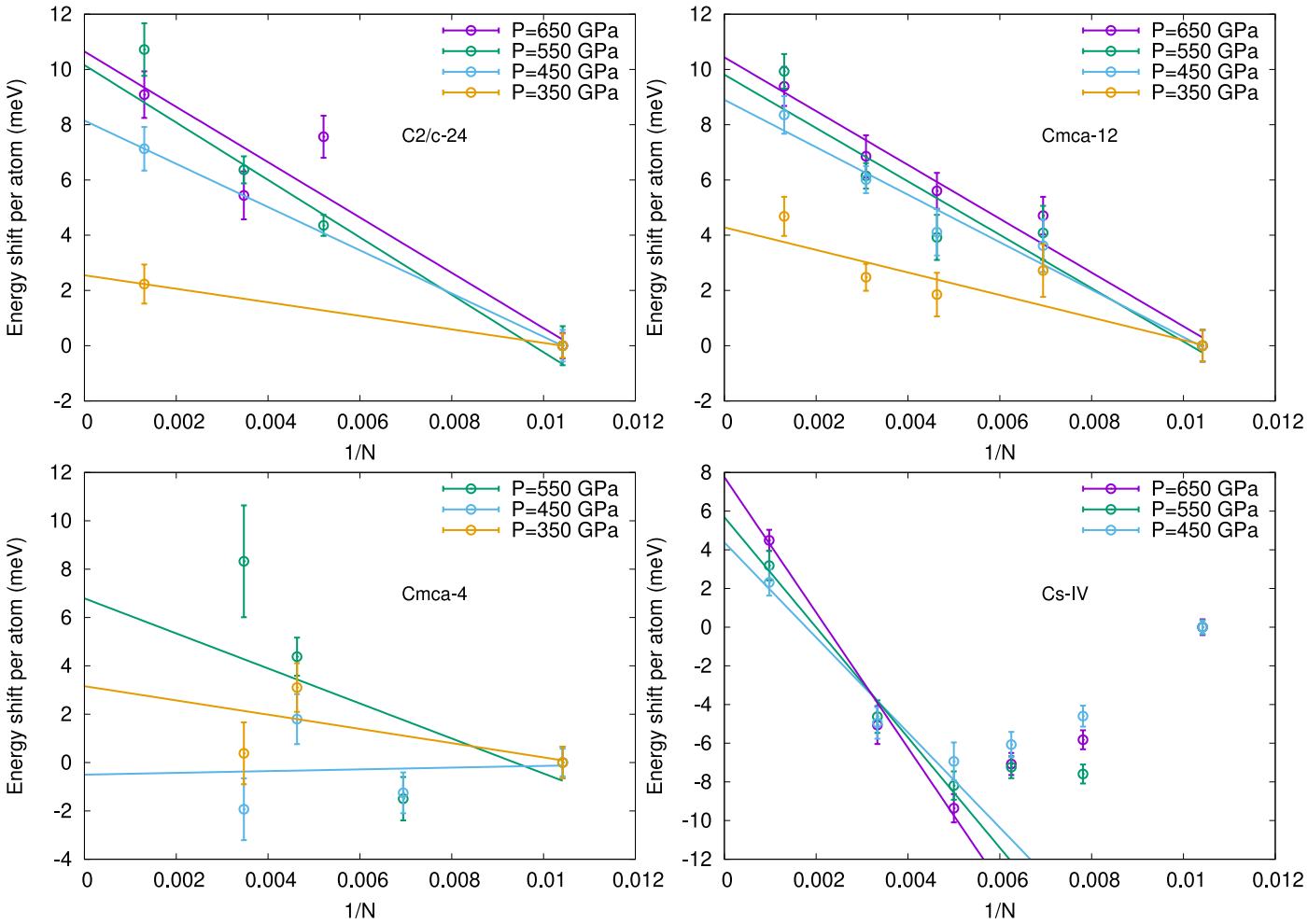

Extended Data Fig. 7 | QMC finite-size scaling and extrapolation to the thermodynamic limit. KZK-corrected lattice-regularized DMC energies for 4 crystalline symmetries (C2/c-24, Cmca-12, Cmca-4, and Cs-IV) plotted as a function of $1/N$, where N is the number of atoms in the supercell, with respect to their value at $N = 96$, taken as reference. The energies are twisted-averaged in the canonical ensemble over a k-grid that has been rescaled according to the size of the supercell, as explained in SI. Note that despite the KZK correction and the canonical k-average, there is a residual size dependence beyond $N = 96$, larger than the target accuracy of ± 1 meV per atom, that needs to be extrapolated. As expected, this residual dependence is stronger in the atomic metallic phase and in the molecular phases under higher pressure, where the metallic character is enhanced.

https://doi.org/10.1038/s41567-023-01960-5

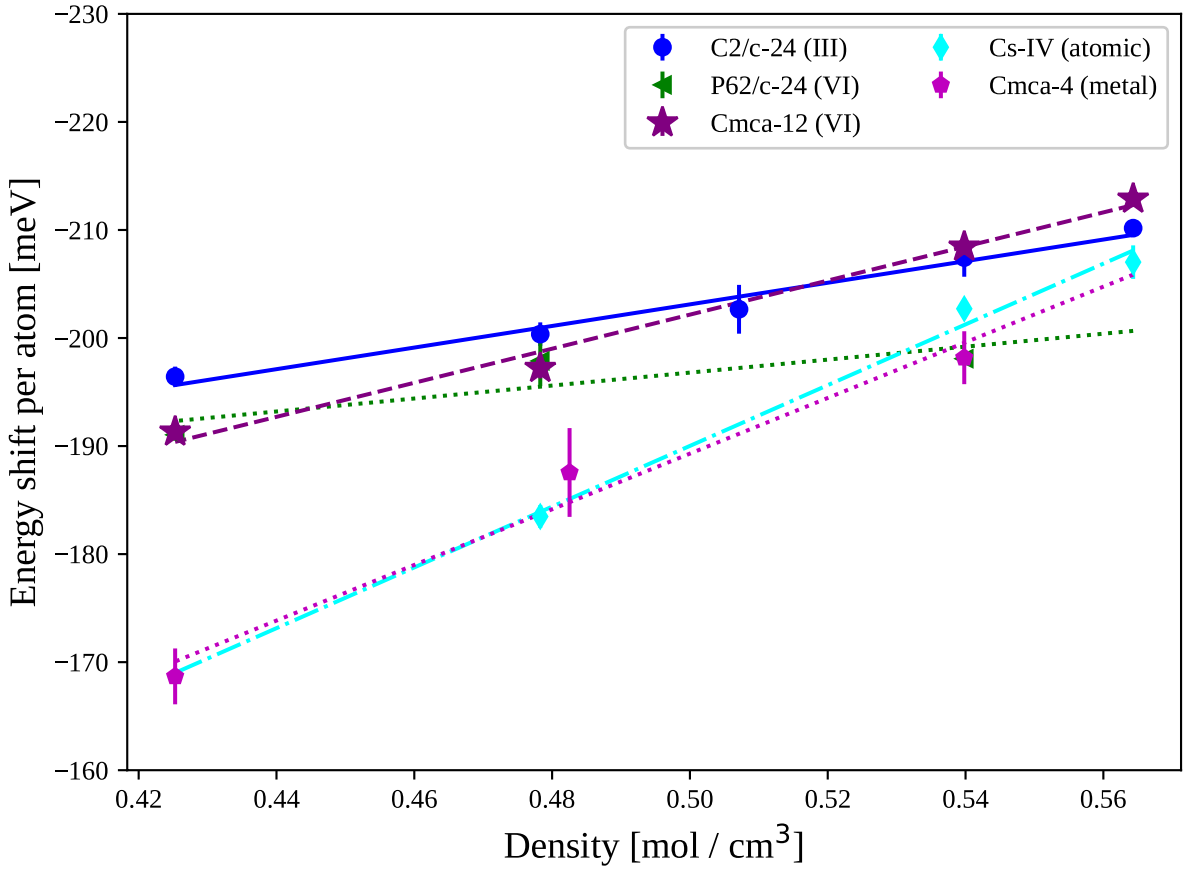

Extended Data Fig. 8 | QMC corrections of DFT-BLYP energies. We plot the electronic energy differences between DFT-BLYP and DMC calculations at hydrogen centroid positions obtained from SSCHA nuclear quantum fluctuations evaluated at the DFT-BLYP level. The DMC energies are computed within the fixed-node approximation with DFT-LDA nodes (see SI for more details). The fit is a straight line for all phases. The absolute value of the shift includes the effect of the pseudopotential.